A new zeolitic hydroxymethylimidazolate material and its use in mixed matrix membranes based on 6FDA-DAM for gas separation

Adelaida Perea-Cachero, Javier Sánchez-Laínez, Ángel Berenguer-Murcia, Diego Cazorla-Amorós, Carlos Téllez, Joaquín Coronas

www.elsevier.com/locate/memsci

PII: S0376-7388(17)31667-8
DOI: http://dx.doi.org/10.1016/j.memsci.2017.09.009
Reference: MEMSCI15547

To appear in: *Journal of Membrane Science*

Received date: 12 June 2017
Revised date: 31 July 2017
Accepted date: 2 September 2017

Cite this article as: Adelaida Perea-Cachero, Javier Sánchez-Laínez, Ángel Berenguer-Murcia, Diego Cazorla-Amorós, Carlos Téllez and Joaquín Coronas, A new zeolitic hydroxymethylimidazolate material and its use in mixed matrix membranes based on 6FDA-DAM for gas separation, *Journal of Membrane Science,* http://dx.doi.org/10.1016/j.memsci.2017.09.009

A new zeolitic hydroxymethylimidazolate material and its use in mixed matrix membranes based on 6FDA-DAM for gas separation

Adelaida Perea-Cachero[a], Javier Sánchez-Laínez[a], Ángel Berenguer-Murcia[b], Diego Cazorla-Amorós[b], Carlos Téllez[a], Joaquín Coronas[a,*]

[a]Chemical and Environmental Engineering Department and Instituto de Nanociencia de Aragón (INA), Universidad de Zaragoza, 50018 Zaragoza, Spain

[b]Alicante Materials Institute and Inorganic Chemistry Department, University of Alicante, 03080 Alicante, Spain

*Corresponding author. coronas@unizar.es

Abstract

The new ZIF named UZAR-S13 is formed by Zn^{2+} and 4(5)-(hydroxymethyl)imidazolate. UZAR-S13 has two distinct phases according to SEM and XRD: amorphous spheres and sheet crystals. UZAR-S13 and byproducts, with no N_2 adsorption, rendered a notable CO_2 uptake (up to 3.8 mmol g^{-1} at 30 bar and 0 °C), approaching values of known ZIFs. The most promising materials were included as fillers in mixed matrix membranes based on copolyimide 6FDA-DAM to study the separation of CO_2/CH_4, CO_2/N_2, H_2/CO_2 and H_2/CH_4. The pore blocking hindered the gas flow of bulky molecules (CH_4, N_2 and CO_2). The high CO_2 adsorption on sheet crystals also contributed to the decrease in the permeability of CH_4, N_2 and CO_2, giving poor selectivities. In contrast, the MMMs improved both the H_2/CH_4 selectivity (8.9-12.7 *vs*. 7.2) and permeability of H_2 (544-597 *vs*. 505 Barrer) of the bare 6FDA-DAM membrane. This emphasizes the potential application of the fillers in the separation by molecular sieving of gas mixtures without CO_2.

Graphical abstract

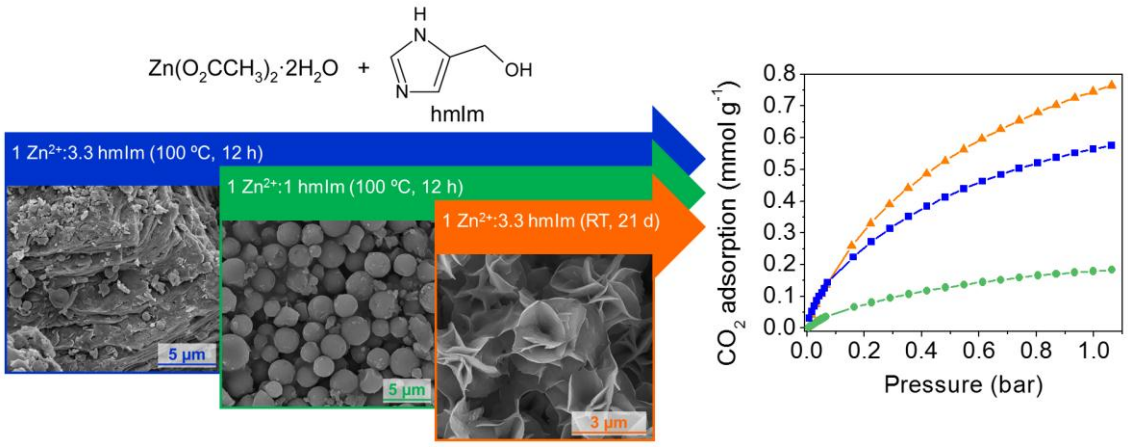

Keywords: MOF, ZIF, copolyimide 6FDA-DAM, mixed matrix membrane, gas separation

1 Introduction

CO_2 is the main greenhouse gas and its accumulation in the atmosphere is causing the so-called global warming phenomenon. The necessity of CO_2 separation has arisen as a consequence of the damage caused by emissions from power generation, industrial processes, de-carbonization and transportation [1]. Carbon capture and storage (CCS) is the principal approach to reduce CO_2 levels in the environment [2, 3]. The crucial stage in this process is the separation of CO_2 from other gases before it reaches the atmosphere [2]. In addition, CO_2 is an impurity present in fuel gases, such as natural gas or biogas, which diminishes the heating value of fuels and causes corrosion in pipelines [4, 5]. In this context, natural gas and H_2 are being explored as alternative energy resources and carriers since they have high heating values [6]. Natural gas, mainly composed of CH_4, is a desirable fuel for transportation [7]. Its combustion produces the least CO_2 emissions per energy since CH_4 is the hydrocarbon with the highest H/C ratio [7]. Natural gas is considered as a transition fuel while H_2 technology is progressing [6]. Promising techniques have been developed to achieve effective CO_2 separation in CCS and natural gas purification as well as CH_4 separation in H_2 purification. Gas separation membranes are considered as a less energy-demanding and more efficient

technology than conventional methods [2, 8, 9]. Commercial gas separation through membrane technology is dominated by polymeric membranes due to their low cost, easy processability and mechanical stability [3, 10]. However, polymeric membranes present a trade-off between permeability and selectivity [10]. In mixed matrix membranes (MMMs), porous particles (fillers) are included in polymers to combine the advantages of both phases, these being high selectivities and permeation fluxes [8, 10]. While zeolites, mesoporous silica and carbon molecular sieves have been widely employed as fillers, metal-organic frameworks (MOFs) and zeolitic imidazolate frameworks (ZIFs) have recently been incorporated into MMMs [11-13].

MOFs, also known as porous coordination polymers (PCPs), are hybrid porous networks formed by the coordination of metal ions or clusters and organic ligands resulting in one-, two- or three-dimensional (1D, 2D or 3D) structures [14]. MOFs feature exceptional surface areas, high pore volumes, considerable thermal and chemical stability, permanent porosity and flexibility [10]. Besides, the broad diversity of metals and organic ligands has given rise to a number of MOFs with different structures and characteristics [15-17]. The size, shape and chemical surface of the pores, and thus the properties of the MOF, can be tailored by selecting the appropriate metallic and organic species [15-17]. ZIFs constitute an interesting subfamily of MOFs. Their framework is composed of divalent metal ions (Zn^{2+}, Co^{2+}, Cu^{2+}, etc.) and imidazolate-type ligands. The coordination of the metallic and organic components gives tetrahedral subunits whose arrangement leads to a zeolitic topology, i.e. the M-Im-M angle (M, metal; Im, imidazolate) in ZIFs and the Si-O-Si angle typically found in zeolites are similar (145°) [18]. Consequently, ZIFs combine properties of both MOFs and zeolites, such as superior thermal and chemical stabilities [19, 20], microporosity [20], large surface areas [19, 20], diversity of frameworks [21], wide range of pore sizes [22], and post-functionalization [21]. All these properties make ZIFs attractive candidates for gas separation, especially by adsorption and membrane technologies [22]. In this respect, ZIFs have shown remarkable CO_2 capacities

[23] and promising separation performances for several binary gas mixtures containing CO_2 which are relevant in different industrial processes [19, 23].

In recent years, the interest in crystalline layered materials has been increasing because their 2D character provides them with extraordinary physicochemical properties [24] such as size- and shape-dependent electronic and optical properties [25], mechanical strength [25], high surface areas [25], and excellent heat conduction [26]. As a consequence, 2D materials are employed in a vast range of applications in fields such as sensing [27], catalysis [27], molecular recognition [28], energy storage [27, 29], (opto)electronics [30] and gas separation [31, 32]. This in turn has provoked the current interest in the preparation of 2D nanostructured MOFs. Layered MOFs could be of great importance for selective gas adsorption [29, 33, 34] since lamellar compounds are able to accommodate guest molecules between the layers [35] while their hybrid nature allows tunable guest-framework interactions [33]. As an example of enhancement with layered MOFs, Rodenas *et al*. prepared MMMs with CuBDC (2D structure) nanosheets as a filler achieving a selectivity between 7.5 and 8 times higher than those of bulk CuBDC MMMs [29]. Moreover, upon delamination, layered MOFs can give rise to ultrathin selective membranes [36].

The synthesis and characterization of UZAR-S13 (henceforth referred to as S13_sph&sh), a new ZIF, is reported here. S13_sph&sh is formed after the reaction at mild temperature of Zn^{2+} and 4(5)-(hydroxymethyl)imidazolate (hmIm, see Figure 1) in a 1:3.3 molar ratio giving rise to two distinct phases related to the shape (spheres and sheets). The hmIm ligand was selected because its hydroxyl functional group was thought to influence the capability of interaction with small gas molecules such as CO_2 [37]. Spheres and sheets are obtained separately by modifying the metal:ligand ratio. Sheet-shaped crystals are also achieved when the reaction is carried out at room temperature maintaining the original metal:linker ratio (S13_sheet_RT). CO_2 adsorption studies at low and high pressure were carried out on these samples. The sheet

shape of crystals of S13_sph&sh and S13_sheet_RT and their CO_2 affinity opened up the possibility of their application in membranes for CO_2 separation. Thus, MMMs were prepared using S13_sph&sh and S13_sheet_RT as fillers and copolyimide 6FDA-DAM as the polymeric matrix. 6FDA (2,2-bis(3,4-carboxyphenyl) hexafluoropropane dianhydride)-based polyimides have shown excellent properties ranging from mechanical strength, chemical and thermal stability, and spinnability to high gas permeability and selectivity [38]. Such good gas permeation properties are produced by the presence of fluorinated side groups (-$C(CF_3)_2$-) (see Figure 1b). These bulky and hydrophobic groups can affect the gas solubility in the membranes, the chain rigidity, the internal rotation of bonds, molecular distances, and the free volume between the polymer chains [39]. The MMMs obtained were employed in the separation of CO_2/CH_4, CO_2/N_2, H_2/CO_2 and H_2/CH_4 mixtures, typical of natural gas, post-combustion, pre-combustion and H_2 purification processes.

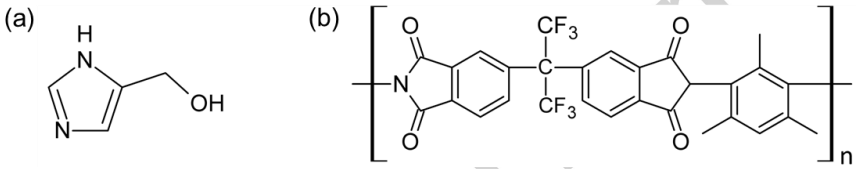

Figure 1. Chemical structure of (a) 4(5)-(hydroxymethyl)imidazole (hmIm-H) and (b) 6FDA-DAM.

2 Experimental section

2.1 Methods and materials

Anhydrous chloroform ($CHCl_3$, ≥99 %, Sigma-Aldrich), *N*,*N*-dimethylformamide (DMF, $HCON(CH_3)_2$, 99.5 %, Scharlau), 4(5)-(hydroxymethyl)imidazole (hmIm-H, $C_4H_6N_2O$, 97 %, Aldrich) and zinc acetate dihydrate ($Zn(CH_3COO)_2{\cdot}2H_2O$, 98 %, Sigma-Aldrich) were used as received without further purification. 6FDA-DAM (418 000 Da) polymer was purchased from

Akron Polymer Systems, Inc. and prepared using the monomers 6FDA and DAM (diaminomesitylene).

2.2 Synthesis of S13_sph&sh

In a typical synthesis, 0.1580 g of zinc acetate dihydrate and 0.2354 g of hmIm-H were dissolved in 8 mL and 10 mL of DMF, respectively (the molar metal:linker ratio was 1:3.3). The metal solution was poured on the ligand solution and the mixture was stirred for 5 min. Subsequently, the resulting solution was placed in a stainless steel Teflon™-lined autoclave. The autoclave was transferred into a conventional oven preheated at 100 °C where it was kept for 12 h. After cooling to ambient temperature, the product was collected by centrifugation at 10 000 rpm and washed 3 times with fresh DMF. Finally, it was dried for 2 d at room temperature.

2.3 Synthesis of S13_sphere_1:1, S13_sphere_1:2, S13_sheet and S13_sheet_RT

In order to obtain separately the spheres and sheets observed in S13_sph&sh, the metal:ligand ratio was modified to 1:10, 1:2 and 1:1 achieving S13_sheet, S13_sphere_1:2 and S13_sphere_1:1, respectively. All these products were prepared and rinsed according to the procedure used for S13_sph&sh. For the same purpose, the synthesis conditions were modified decreasing the temperature and augmenting the reaction time, but keeping the metal:linker ratio from S13_sph&sh, giving S13_sheet_RT. In this case, the hmIm solution was prepared in a glass vial. Then the metal solution was added. The mixture was stirred for 5 min. The reaction was carried out under static conditions at room temperature. After 21 d, the product was recovered by centrifugation at 10 000 rpm, washed 3 times with DMF and dried at ambient conditions. Yields of these products as well as that of S13_sph&sh are presented in Table S1. The yields were calculated as an average of at least two syntheses. It is worth mentioning that a reaction time of 14 d in the synthesis of 1_sheet_RT gave the same kind of

sheets but slightly smaller. Thus we chose 21 d in order not to prolong excessively the reaction time, believing that the size of the sheets would hardly have changed with longer times.

2.4 Activation of S13_sph&sh, S13_sphere_1:1 and S13_sheet_RT

Samples S13_sph&sh, S13_sphere_1:1 and S13_sheet_RT were activated by means of a solvent-exchange process. First, the products were immersed in anhydrous chloroform at room temperature under stirring. The chloroform was refreshed every 24 h. After 7 d, the solvent was removed by centrifugation. The solids were rinsed 3 times with fresh chloroform and dried at ambient conditions. They were then treated under vacuum at 80 °C (140 °C in the case of S13_sphere_1:1) for 8 h with heating and cooling rates of 1 °C min^{-1}, producing S13_sph&sh_act, S13_sphere_1:1_act and S13_sheet_RT_act. The elemental analysis calculated for S13_sph&sh_act ($Zn(C_4H_5N_2O)_2 \cdot H_2O = C_8H_{12}N_4O_3Zn$), i.e. C, 34.62; H, 4.36; N, 20.18, was in good agreement with the values experimentally found by elemental analysis, i.e. C, 36.74; H, 4.67; N, 19.97.

2.5 MMM preparation

Prior to MMM preparation, 6FDA-DAM in thread form was dried at 100 °C overnight. Samples S13_sph&sh and S13_sheet_RT were employed as recovered after chloroform exchange (before vacuum treatment). The solids were dispersed in anhydrous chloroform in such a way that the ZIF loading in the polymeric matrix was 10 wt%. The calculated amount of 6FDA-DAM was then added. The mixture was stirred overnight. The casting solution was subjected to three cycles of sonication and stirring (the sonication and stirring lasted 15 minutes each in each cycle). The suspension was cast into a Petri dish at room temperature. The Petri dish was capped so that the solvent slowly evaporated. Occluded chloroform molecules were readily removed upon heating at 100 °C for 1 d. The membranes prepared with the pure polymer, S13_sph&sh and S13_sheet_RT had a thickness of 64 ± 13 µm, 68 ± 8 µm and 74 ± 3 µm, as

measured with a Digimatic Micrometer. These values were determined by averaging the results of the same kind of membranes after 3-4 measurements per membrane.

2.6 Binary gas separation experiments

Permeability tests were carried out to study the separation performance of the MMMs prepared in this work. The membranes, 3.14 cm^2 in area, were supported on a 316LSS macroporous disk inside a stainless steel module and gripped with Viton® O-rings. The macroporous support had a nominal pore size of 20 µm and was purchased from Mott Corporation. Experiments were carried out at 35 °C inside an oven to control the temperature. Equimolar CO_2/CH_4, H_2/CO_2 and H_2/CH_4 and 10/90 vol% CO_2/N_2 gas mixtures were fed into the module at 3.0 bar through two mass-flow controllers (Alicat Scientific, MC-100CCM-D) with a total volumetric flow of 50 and 100 cm^3(STP) min^{-1}, respectively. The permeate side was swept at 1.2 bar with a 2 cm^3(STP) min^{-1} stream of He (4.5 cm^3(STP) min^{-1} for the pure 6FDA-DAM membrane) regulated by a mass-flow controller (Alicat Scientific, MC-5CCM-D). The permeate stream was analyzed by means of an Agilent 3000A online gas microchromatograph equipped with a thermal conductivity detector (TCD) to determine the concentration of both gas components. Measurements were taken once the steady state was achieved (at around 1.5 h). Permeability values were expressed in Barrer units (1 Barrer = 10^{-10} cm^3(STP) cm (cm^{-2} s^{-1} $cmHg^{-1}$) = 7.5 x 10^{-18} m^3(STP) m (m^{-2} s^{-1} Pa^{-1})). Membrane selectivity, $S_{i/j}$, was calculated as the ratio of the permeability of the component *i* over that of the component *j*.

2.7 Characterization

Fourier transform infrared (FTIR, Shimadzu IRAffinity-1) spectra of bulk samples were recorded using the KBr disk technique in a wavenumber range of 4000-400 cm^{-1}. Attenuated total reflectance Fourier transform infrared (ATR-FTIR, Bruker Vertex 70 FTIR) spectra of the MMMs were recorded between 4000 and 600 cm^{-1}. The resolution of both FTIR and ATR-FTIR spectra was 4 cm^{-1}. Thermogravimetric analyses (TGA, Mettler Toledo TGA/DSC 1 SF/755) were

performed with a heating ramp of 5 °C min^{-1} from 25 to 900 °C in air atmosphere. The glass transition temperature (T_g) of the MMMs was determined by differential scanning calorimetry (DSC, Mettler Toledo DSC822^e). The MMMs were scanned in two consecutive runs from 25 to 450 °C using a heating rate of 20 °C min^{-1} in air. The value of T_g was calculated from the heat flow curve as the temperature in the inflexion point of the second run in order to remove the thermal and mechanical history of the samples. Bulk products as well as the MMMs were characterized by powder X-ray diffractometry (PXRD, D-Max Rigaku and Bruker D8 Advance). PXRD patterns were gathered at ambient temperature with a copper anode using a graphite monochromator to select CuKα radiation with λ = 1.5418 Å. Scanning electron microscopy (SEM, FEI Inspect F50) studies of the samples were carried out in a voltage range of 2-5 kV. The samples were coated with platinum under vacuum conditions. For cross-section SEM images of the MMMs, small pieces of membranes were broken inside a liquid N_2 bath (freeze-fracturing) to produce a clean cross sectional surface. Crystal thicknesses were measured by means of the ImageJ [40] software using SEM images. Brunauer-Emmett-Teller (BET) specific surface areas were determined from N_2 sorption isotherms at -196 °C (Tristar 3000). CO_2 adsorption isotherms at low pressure (Micromeritics ASAP 2020 V1.04H) were collected at 25 °C. Samples (*ca*. 150 mg) for CO_2 (low pressure) and N_2 sorption were previously degassed at 80 °C for 8 h with a heating rate of 1 °C min^{-1}. High pressure carbon dioxide and hydrogen adsorption measurements were done in an automatic volumetric apparatus (Quantachrome iSorb HP1) to perform carbon dioxide isotherm experiments up to 45 bar and hydrogen isotherm experiments up to 200 bar. The manifold of the apparatus was kept at 36 °C. For the CO_2 experiments, a circulator bath set to 0 or 40 °C was employed to ensure a constant adsorption cell temperature. In the case of hydrogen, the sample cell was kept at 25 °C by means of a liquid bath. The manifold volume was calibrated with a standard volume, using helium as a calibrating fluid. To ensure that the apparatus was leak-free, hydrogen leak tests were executed at 90 and 150 bar for 28 h, the resulting leak rate being below 10^{-6} Torr ($Torr^{-1}$ s^{-1}).

The bulk gas amounts were obtained using the modified Benedict-Webb-Rubin equation of state [41] and the cell volume was obtained considering the correction described in the literature [42]. Prior to all the adsorption experiments, the samples were degassed at 150 °C for 4 h under vacuum. After that, the sample was loaded in the sample holder, and then evacuated at 150 °C for another 4 h under vacuum. Sample masses ranged between 0.5 and 1.0 g to ensure accurate measurements. Excess adsorption was obtained in both CO_2 and H_2 sorption measurements at high pressure. Elemental analysis (Thermo Flash 1112) was carried out to reveal the C, H and N composition of the samples.

3 Results and discussion

3.1 Characterization of S13_sph&sh, S13_sphere_1:1, S13_sphere_1:2, S13_sheet and S13_sheet_RT

The chemical formula of ZIFs is commonly $M(Im)_2$ (where Im denotes any type of imidazolate ligand) [43, 44]. The formula of S13_sph&sh, established taking into account the results obtained in TGA characterization, is $Zn(hmIm)_2 \cdot xDMF \cdot yH_2O$, where typically x = 0.15 and y = 1.0. In the case of S13_sph&sh_act, elemental analysis and TGA data were used to corroborate its chemical formula: $Zn(hmIm)_2 \cdot zH_2O$ (normally, z = 0.5). Calculations were carried out using TGA curves of 4 and 5 samples for S13_sph&sh and S13_sph&sh_act, respectively. The different values acquired from the thermograms were utilized as an average in order to achieve an accurate solution. Figure 2 shows the TGA and differential thermogravimetric (DTG) curves of S13_sph&sh and S13_sph&sh_act. The first weight loss at 25-100 °C in both samples is due to water release and has a value of 6.2 and 3.6 % (calcd. 6.2 and 3.2 %), respectively. In S13_sph&sh, a second step of 3.4 % between 100 and 175 °C is found and is attributed to DMF loss (calcd. 3.8 %). S13_sph&sh_act does not possess such a step. The decomposition of both samples takes place from *ca*. 175 °C. FTIR characterization corroborates the presence of a small amount of DMF molecules in S13_sph&sh (Figure S1). The band placed at 1660 cm^{-1} is ascribed to the C=O stretching from DMF [45]. This band disappeared for S13_sph&sh_act. This confirms that S13_sph&sh_act was successfully activated, as expected from the TGA results.

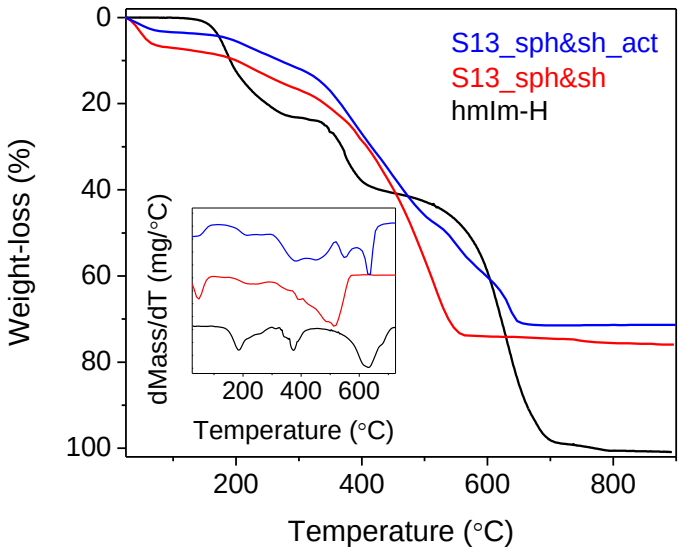

Figure 2. TGA and DTG curves of hmIm-H, S13_sph&sh and S13_sph&sh_act.

As shown in the SEM images (and confirmed by PXRD patterns), two phases are well-differentiated in S13_sph&sh (Figure 3a). The first is composed of spherical particles with a size ranging between 0.7 and 2.5 µm. The second and majority phase contains large layers composed of sheet blocks with edges of around 1 µm (see inset).

In order to obtain both phases separately, different syntheses were carried out varying the molar metal:ligand ratio. The ratio for S13_sph&sh had a value of 1:3.3. When this was increased up to 1:2 and 1:1 (S13_sphere_1:2 and S13_sphere_1:1), only spheres were obtained (Figure 3b and 3c). The size distribution is heterogeneous with particles larger than spheres of S13_sph&sh (approximately 1.0-5.5 µm in diameter). It is worth mentioning that S13_sphere_1:1 is a purer phase than S13_sphere_1:2, as observed by microscopy (and verified by PXRD), because the latter has a larger number of irregular particles along with the spheres. On the other hand, diminishing the metal:linker ratio down to 1:10 led to rectangular sheets with round vertices and submicrometric edges (Figure 3d). Flat particles were also obtained when the synthesis conditions were adjusted keeping the molar ratio of S13_sph&sh

(S13_sheet_RT). The reaction at room temperature for 21 d gives rise to larger sheets (1.0-3.5 µm). After drying at ambient conditions, crystals exposed to the atmosphere were arranged forming rosettes (Figure 3e) while crystals in contact with the glass dish were arranged with the larger face parallel to the surface (Figure 3f).

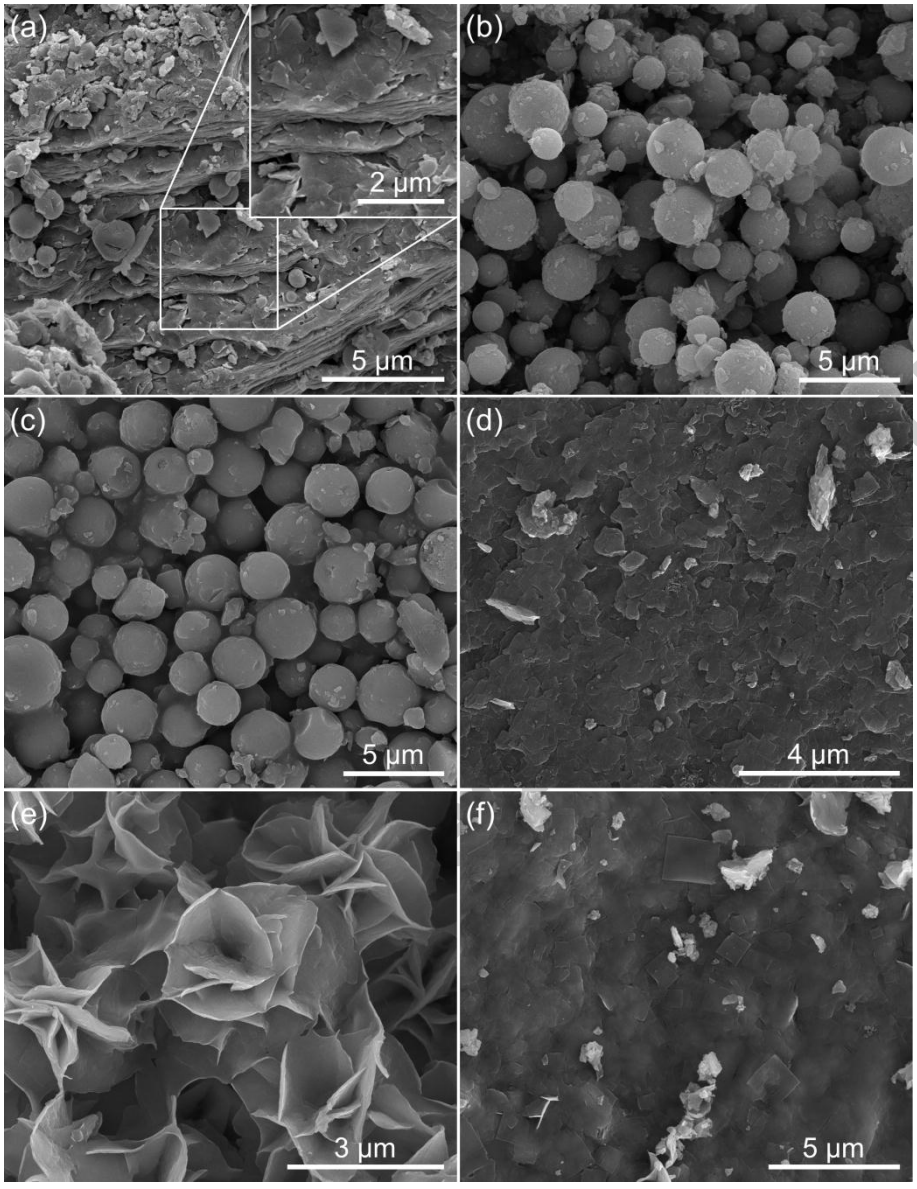

Figure 3. SEM images of (a) S13_sph&sh, (b) S13_sphere_1:2, (c) S13_sphere_1:1, (d) S13_sheet, (e) crystals of S13_sheet_RT exposed to the atmosphere (rosettes) and (f) in contact with dish surface.

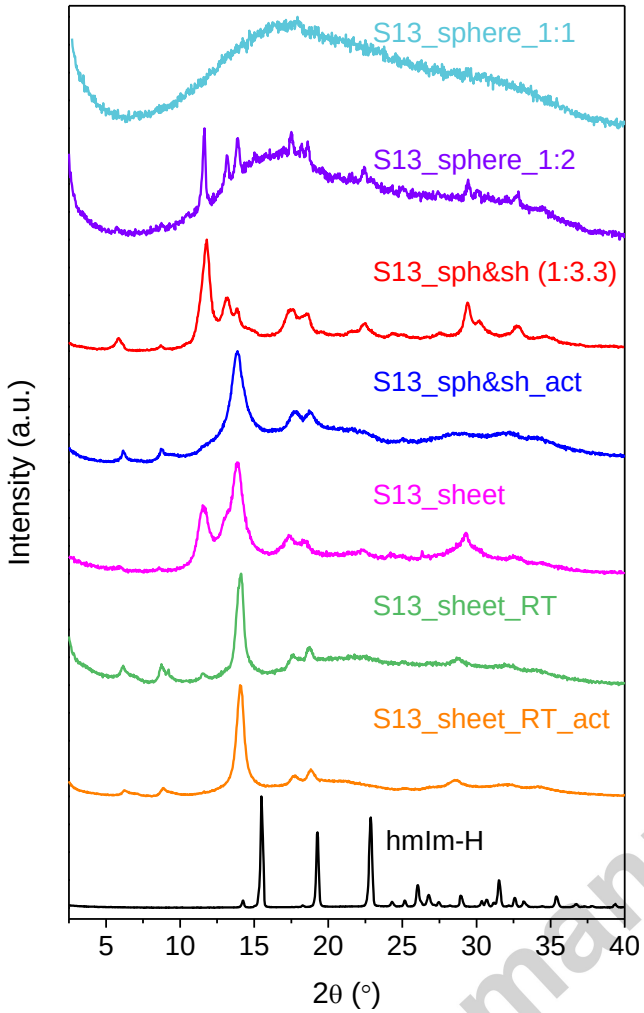

Figure 4. PXRD patterns of some products synthesized in this study and that of hmIm-H. The molar metal:ligand ratio of S13_sph&sh is shown between parentheses.

PXRD patterns of the samples prepared in this work are depicted in Figure 4. It was not possible to solve their crystal structures by single crystal X-ray diffraction as single crystals were not obtained. PXRD data was not useful either, because of the scarcity of diffraction peaks and their broad width. As mentioned above, PXRD studies corroborate that S13_sph&sh possesses two distinct phases: spheres and sheets. The spheres (S13_sphere_1:2 and S13_sphere_1:1) constitute an amorphous phase whereas the sheets (S13_sheet) define the crystalline phase. S13_sheet and S13_sph&sh_act maintain the peak positions from

S13_sph&sh (see Figure 4), although the relative intensities change, probably due to a shift in crystal orientation. This is clearly seen in the SEM images of S13_sheet (Figure 3d), where the flat faces from the crystals are parallel to the sample holder. In the case of S13_sph&sh_act, the modification in intensity could also be caused by the break of layered blocks during activation (Figure S2a and b). The SEM appearance of S13_sheet_RT and S13_sheet_RT_act (Figure S2c and d) are similar to those of S13_sheet and S13_sph&sh_act owing to the flat arrangement of the particles. Finally, Figure 3 and Figure S2 also show the filler particles (S13_sph&sh and S13_sheet_RT) before and after activation with no evidences of appearance changes.

FTIR spectra of S13_sheet, S13_sphere_1:2, S13_sphere_1:1 and S13_sheet_RT are displayed in addition to that of S13_sph&sh in Figure S1. The S13_sheet and S13_sheet_RT spectra, corresponding to samples containing crystals with flat morphology, are in good agreement with that of S13_sph&sh (sheets and spheres). However, S13_sphere_1:2 and S13_sphere_1:1 have broad bands at around 1580-1600 cm^{-1} and between 1438 and 1360 cm^{-1} (rectangles in Figure S1). According to SEM inspection, the latter samples correspond to spheres. This implies that the composition of the amorphous phase, i.e. spheres, is different from that of S13_sph&sh. However, the presence of the amorphous phase in S13_sph&sh is barely perceptible by FTIR analysis, so that a negligible contribution to the properties of S13_sph&sh would be expected.

Sorption experiments of CO_2 and N_2 at low pressure were performed on S13_sph&sh_act, S13_sphere_1:1_act and S13_sheet_RT_act (Figures 5a and S3). According to FTIR spectra (Figure S1), the band typical of DMF was not visible for these products, thus they were well-activated. Despite the low BET specific surface areas (5-12 $m^2 g^{-1}$, see Table 1), the CO_2 adsorption capacities are relatively significant when compared with values from other ZIFs [46-50], especially those of S13_sph&sh_act and S13_sheet_RT_act (see Table 1). This is due to the

sheet crystals, whose 2D nature favors selective CO_2 adsorption. S13_sheet_RT_act (0.7 mmol g^{-1}) with an uptake similar to that of ZIF-8 almost reached the uptake values of ZIF-97 (1.0 mmol g^{-1}) [49] and ZIF-L (0.9 mmol g^{-1}) [47]. The latter ZIFs are somewhat similar to UZAR-S13 materials because ZIF-97 (3.08-3.65 Å in aperture size; 16.5 Å in pore diameter) [51] includes in its framework a ligand similar to hmIm (Figure S3) whereas ZIF-L (pore size of 9.4 x 7.0 x 5.3 $Å^3$) nanoflakes possess a 2D structure [52]. On the other hand, ZIF-9 (4.31 Å in pore diameter) and ZIF-11 (14.6 Å) do not show N_2 adsorption because their aperture sizes (2.9 and 3.0 Å, respectively) are smaller than the kinetic diameter of N_2 (3.64 Å) [49], but they exhibit structural flexibility due to ligand rotation which allows adsorbates to reach the pores (gate-opening) [53, 54]. The UZAR-S13 type materials adsorb CO_2 but not N_2. It is supposed that these materials have a pore aperture between the kinetic diameters of CO_2 (3.3 Å) and N_2 in such a way that N_2 molecules cannot reach the pores because they are too large whilst CO_2 fits the pore aperture and is able to enter the pores. Another hypothesis is that the UZAR-S13 materials have a pore aperture below the kinetic diameter of CO_2 and their flexible structure allows the hmIm ligands to rotate upon CO_2 adsorption, thus CO_2 molecules entering the pores, as occurs in ZIF-9 and ZIF-11. The CO_2 adsorption would be enabled in both cases. The ZIFs summarized in Table 1, except ZIF-9 and ZIF-11, show significant BET surface areas because their pore apertures or dimensions exceed the size of the N_2 molecule or, when the pore apertures are slightly lower, because of the mentioned gate-opening effect [53, 54] upon N_2 sorption. The lower CO_2 capacity of S13_sphere_1:1_act arose from its amorphous character, rendering more disordered and less accessible pores. This provoked less CO_2 sorption on S13_sph&sh_act, constituted by spheres and sheets, compared to that of S13_sheet_RT_act, formed only by sheets. Therefore, the amorphous contribution to S13_sph&sh, not noticed by the FTIR studies, was evidenced by CO_2 adsorption.

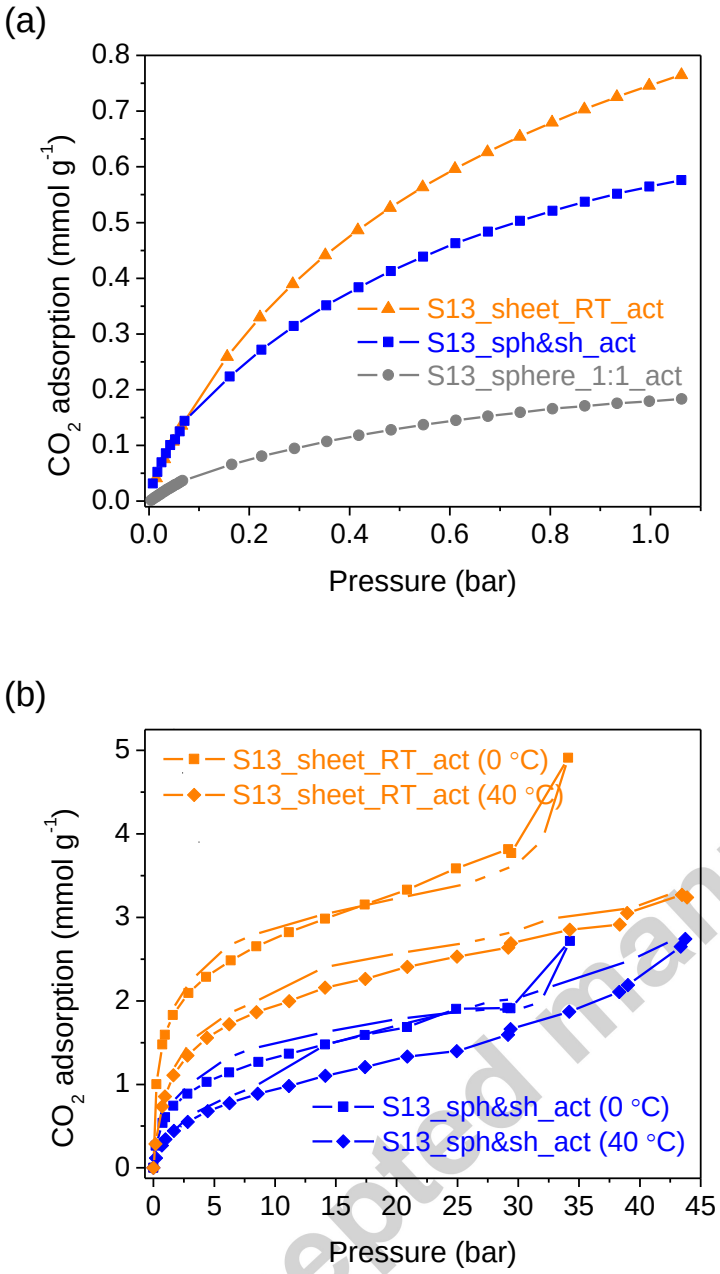

Figure 5. CO_2 adsorption isotherms at (a) low pressure (25 °C) and (b) high pressure (0 and 40 °C) of S13_sph&sh_act, S13_sheet_RT_act and S13_sphere_1:1_act (only adsorption at low pressure). High pressure adsorption corresponds to the adsorption excess. Filled and open symbols for adsorption and desorption, respectively.

Table 1. CO_2 adsorption capacities for selected ZIFs

MOF	BET surface area ($m^2\ g^{-1}$)	Capacity ($mmol\ g^{-1}$)	(wt%)	P (bar)	T (°C)	Reference
ZIF-9 (bIm)	4	2.7	-	1	0	[54, 55]
ZIF-11 (bIm)	-	2.05	-	1.1	0	[53]
ZIF-25 (dmIm)	1110	1.1	-	1	25	[49]
ZIF-71 (dcIm)	652	0.6	-	1	25	[49]
ZIF-93 (almIm)	864	1.6	-	1	25	[49]
ZIF-96 (cyamIm)	960	2.1	-	1	25	[49]
ZIF-97 (hymIm)	564	1.0	-	1	25	[49]
ZIF-L (mIm)	161	0.9	-	1	25	[47]
nZIF-8	1268	-	35.0	30	25	[50]
ZIF-8	1450	0.7	-	1	25	[46]
	1070	*ca*. 5.9[a]	-	30	25	[48]
S13_sphere_1:1_act	5	0.2	0.8	1	25	This work
S13_sph&sh_act	12	0.6	2.5	1	25	This work
		1.9	8.4	30	0	
		2.2	9.6	40	40	
S13_sheet_RT_act	8	0.7	3.4	1	25	This work
		3.8	16.6	30	0	
		3.1	13.4	40	40	

[a] Value taken from the CO_2 isotherms of the corresponding reference.

bIm, benzimidazole; dmIm: 4,5-dimethylimidazole; dcIm: 4,5-dichloroimidazole; almIm: 4-methylimidazole-5-carbaldehyde; cyamIm: 4-aminoimidazole-5-carbonitrile; hymIm: 4-hydroxymethyl-5-methylimidazole; mIm: 2-methylimidazole.

H_2 physisorption measurements were performed on S13_sph&sh_act (Figure S4). H_2 sorption resulted in an uptake of 0.12 wt% at 180 bar, indicating a poor interaction with H_2 molecules. S13_sph&sh_act and S13_sheet_RT_act, the more promising materials, were tested for CO_2 sorption at high pressure and two distinct temperatures (0 and 40 °C) (Figure 5b). High pressure isotherms were in good agreement with those obtained at subatmospheric pressures. Most of the CO_2 molecules were adsorbed below 10 bar; above this pressure, the corresponding uptakes were less significant for both temperatures and products.

As we have reported earlier for carbon-based materials [56], mesoporous materials [57], and even ZIFs [53], CO_2 adsorption at high pressures is a very useful technique given that (1) it

enables characterization of narrow porosity (i.e. pores of sizes around 3 Å, which correspond to the narrower cavities found in ZIF-11) and (2) the isotherms are measured up to relative fugacities close to unity [56] at both temperatures (0 and 40 °C), which allows the whole range of porosity to be covered. One interesting feature is that a steep increase in the adsorption capacity is observed for both samples at 0 °C and pressures above 25 bar, which may be ascribed to CO_2 condensation in intercrystalline (or interlamellar) spaces, as we have reported previously [53]. This phenomenon is not observed for sample S13_sheet_RT_act at 40 °C. Adsorption and desorption branches nearly overlap for all the samples except for S13_sph&sh_act at 40 °C, which shows a noticeable hysteresis cycle from 43 to 10 bar. This hysteresis cannot be related to capillary condensation since this would only occur in the highest pressure region [53, 56]. It could be due to a strong interaction between the CO_2 molecule and the adsorbent or to a change in size or morphology of the pores at high pressures, trapping the CO_2 in its structure.

As seen in table S2, CO_2 capacities (up to 3.8 mmol g^{-1} at 30 bar and 0 °C in the case of S13_sheet_RT_act), even if significant, are below the values for other MOFs. For instance, HKUST-1, containing open metal sites that could enhance CO_2 adsorption [58], adsorbs three times the value of S13_sheet_RT_act. When compared to nZIF-8 and ZIF-8 (Table 1), S13_sph&sh_act and S13_sheet_RT_act exhibit between a third and a half, respectively, of CO_2 capacity despite the fact that their BET areas are around 90-160 times smaller. This underlines the great potential of the 2D crystals of ZIFs S13_sph&sh_act and S13_sheet_RT_act as CO_2 adsorbents. As in the case of CO_2 adsorption at low pressure, uptakes for S13_sheet_RT_act are higher than those of S13_sph&sh_act. This highlights the effect of the amorphous spheres in S13_sph&sh.

3.2 MMM characterization and performance

Following the promising CO_2 adsorption results achieved with S13_sph&sh and S13_sheet_RT, both products were embedded in 6FDA-DAM for MMM fabrication. A ZIF loading of 10 wt% was chosen (even though 20 wt% loading membranes were prepared and tested out of range gas separation performance). The membranes were characterized by SEM, ATR-FTIR and PXRD.

SEM images of the cross section of the MMMs prepared in this work show the ZIF-polymer interaction and the filler distribution in the polymeric matrix (Figure 6). Both S13_sph&sh and S13_sheet_RT are uniformly distributed all over the cross section of the MMMs. Particles of S13_sph&sh and S13_sheet_RT are located in the cavities delimited by the polymeric nerves. Besides, crystals of S13_sheet_RT seem to be preferentially oriented parallel to the MMM surface. The insets shown in Figure 6 reveal a good ZIF-polymeric matrix interaction for both S13_sph&sh and S13_sheet_RT.

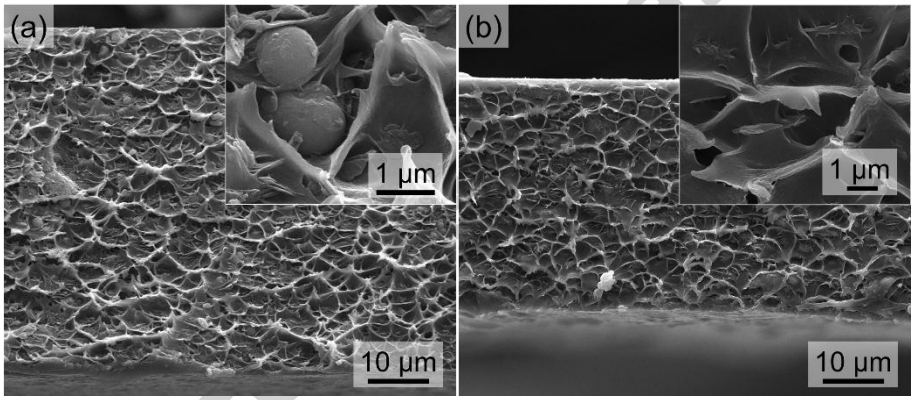

Figure 6. Cross-section SEM images of the MMMs prepared with (a) S13_sph&sh and (b) S13_sheet_RT as fillers.

The ATR-FTIR characterization (Figure S5) shows no difference between the spectra from the bare membrane and the two MMMs. Only bands related to 6FDA-DAM are seen. This is due to the low ZIF loading of the MMMs (10 wt%).

The thermogram of the neat 6FDA-DAM membrane show a weight loss of 2.8 % below 75 °C, attributed to the removal of water molecules adsorbed from the atmosphere (Figure S6). The small decreasing trend (0.6 %) from 75 °C to degradation (around 380 °C) corresponds to chloroform release. This low percentage indicates that the neat membrane was successfully activated. The weight loss of 0.8 and 1.5 % between 25-125 °C for S13_sph&sh/6FDA-DAM and S13_sheet_RT/6FDA-DAM MMMs is probably due to chloroform and water removal. These insignificant values confirm the success in activating the MMMs. The step at 125-285 °C for both membranes (1.2 and 1.4 %, respectively) is ascribed to the filler presence. The decomposition of the MMMs takes place above 380 °C, as that of the bare polymer. DSC experiments were carried out to determine the T_g of the distinct membranes (Table 2). The bare 6FDA-DAM shows a T_g within the reported values for the same polymer (Table S3). As seen, the T_g rises from 384.1 °C for the pure polymer to 400.2 and 399.9 °C for S13_sph&sh/6FDA-DAM and S13_sheet_RT/6FDA-DAM, respectively. As expected, the glass transition temperatures for S13_sph&sh and S13_sheet_RT are similar because both fillers share the same nature. The increase in T_g (about 16 °C) was caused by the rigidification of the polymer, i.e. the movement of the polymer chains surrounding the filler particles was restricted because of chemical interactions between both components [59, 60]. The calculated T_g could show the effect of the corresponding decomposed fillers.

Table 2. Glass transition temperatures and d-spacings (calculated by Bragg's law) for the membranes prepared in this work

Membrane	T_g (°C)	d-spacing (Å)
Bare 6FDA-DAM	384.1	7.0
S13_sph&sh/6FDA-DAM	400.2	6.3
S13_sheet_RT/6FDA-DAM	399.9	6.4

X-ray diffractometry revealed amorphous and broad bands centred at the 2θ values of 13.6° and 13.8° for the S13_sph&sh/6FDA-DAM and S13_sheet_RT/6FDA-DAM MMMs, respectively

(Figure S7). The displacement of the amorphous band from the bare 6FDA-DAM (2θ = 12.7°) towards higher 2θ angles involves a decrease in the d-spacing (7.0 Å *vs*. 6.3 and 6.4 Å, see Table 2). Because of the similarity of the fillers, the corresponding d-spacings barely differ. The d-spacing is related to the interchain distance [61], giving an indication of the packing density of the polymer chains [59]. Thus, lower d-spacings imply a strong filler-polymer interaction which would reduce the distance between the polymeric chains [62]. However, the lower d-spacing could hamper the diffusion of small molecules through the membranes, producing lower permeabilities [59, 61]. The d-spacing for the pure 6FDA-DAM membrane is somewhat higher than the values found in the literature (Table S3). The reflection at 2θ = 14.4° of the S13_sheet_RT/6FDA-DAM membrane is related to the strong peak at 2θ = 14.1° from the filler, corroborating the preservation of its crystallinity. In addition, some parallel preferential orientation of the filler sheets to the membrane itself may provoke the disappearance of certain minor intensities, as observed for other MMMs with lamellar fillers [63]. In the case of the S13_sph&sh/6FDA-DAM membrane, a weak signal at 2θ = 8.6° is ascribed to S13_sph&sh (2θ = 8.7°). The filler-polymer interaction caused changes in the crystal lattice of S13_sph&sh and S13_sheet_RT, producing these shifts in the peak positions to lower or higher angles.

As mentioned in the Experimental section, the activation of the UZAR-S13 materials was carried out by a solvent-exchange process for 7 d with anhydrous chloroform and a subsequent vacuum treatment at 80 °C for 8 h. Nonetheless, the activation of the MMMs was performed at 100 °C for 1 d without vacuum. In order to confirm that the fillers supported the conditions used in the activation of the membranes, a sample of S13_sph&sh was soaked in anhydrous chloroform for 7 d and was then treated at 100 °C for 1 d (S13_sph&sh_100°C). The PXRD pattern, FTIR spectrum and SEM images of S13_sph&sh_100°C are shown in Figure S8, Figure S9 and Figure S2 (e and f), respectively. The FTIR spectrum agrees with that of S13_sph&sh_act and the particle morphologies of both samples were similar. The higher difference was found by PXRD. S13_sph&sh_act and S13_sph&sh_100°C share the same

structure, but the peaks of S13_sph&sh_100°C are broader and less defined. Thus, the activation of the MMMs might have damaged slightly the structure of the fillers.

Given the affinity of the fillers towards CO_2, the S13_sph&sh/6FDA-DAM and S13_sheet_RT/6FDA-DAM MMMs were applied to separate several CO_2 containing mixtures typical of post-combustion, pre-combustion and natural gas purification processes: CO_2/N_2, CO_2/H_2 and CO_2/CH_4, respectively. The 6FDA-DAM polymer is highly permeable, especially towards CO_2. This could affect significantly the permeation results [64].

The distinct sorption studies carried out (described above) could help to understand the gas separation results. Four facts are concluded from the H_2, CO_2 and N_2 sorption. (1) N_2 molecules are unable to enter into the pores of S13_sph&sh and S13_sheet_RT because the kinetic diameter of N_2 is bigger than the pore aperture of the fillers. (2) The interactions between H_2 molecules and the pore walls of S13_sph&sh and S13_sheet_RT are weak. (3) The pores of the 2D crystals in both fillers have a noticeable affinity towards CO_2. (4) As S13_sheet_RT does not contain amorphous spherical particles, its CO_2 uptake is higher.

Permeability and selectivity data are depicted in Figure 7 and Table S4. The permeabilities of H_2, CH_4 and N_2 for the bare 6FDA-DAM match well with those reported in the literature [59, 65], although the permeability of CO_2 (1237-1289 Barrer) is around twofold in comparison with the value obtained by Zornoza *et al*. (mixed gas permeability, 604-681 Barrer) [65] and 1.5-fold with respect to that reported by Qiu *et al*. (single gas permeability, 842 Barrer) [59]. In contrast, the results presented by Boroglu and Yumru [61] and Kim *et al*. [66] (CO_2 single gas permeabilities of 20.6 and 299 Barrer, respectively) are much lower than the values obtained here.

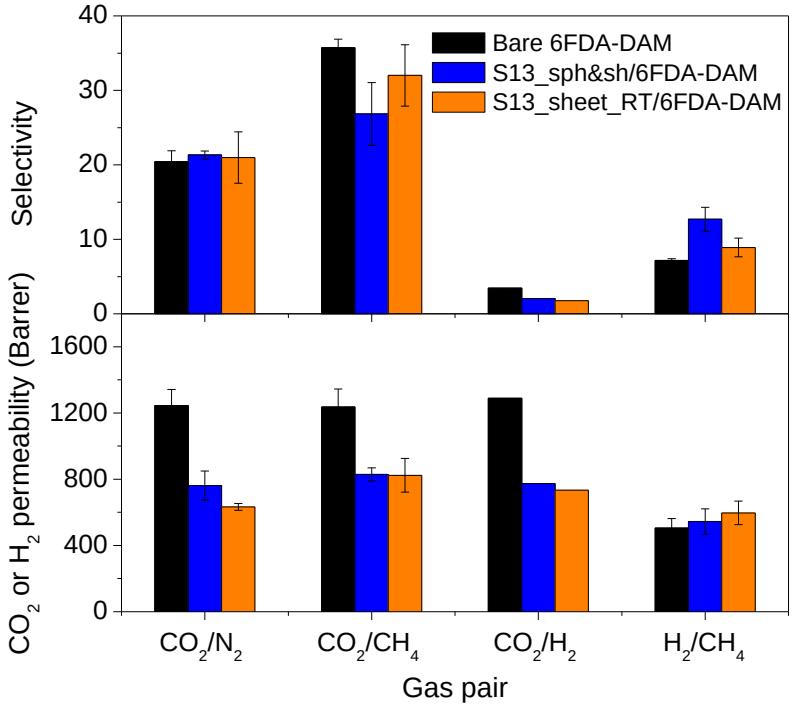

Figure 7. Permeability and selectivity results for the bare 6FDA-DAM membrane, S13_sph&sh/6FDA-DAM and S13_sheet_RT/6FDA-DAM. Error bars indicate the standard deviation of at least two membranes.

Figure 7 shows that the permeabilities of CO_2, N_2 and CH_4 decreased as compared to that of the neat polymer for the three gas pairs whereas only the permeability of H_2 increased (see also Table S4). These reductions (for all the gases except H_2) suggest that the MMMs are defect-free without interface voids, indicating a good polymer-filler contact, as observed by SEM (Figure 6). Interface voids would cause a large increase in permeability for all the gases and non-selective flows [67, 68].

There are five main explanations for the decrease in permeability. (1) As stated above, 6FDA-DAM is highly permeable to gases, especially to CO_2, so that the use of less permeable fillers would lead to lower gas permeabilities through the MMMs. (2) A higher tortuosity due to the filler presence in the polymeric matrix disturbs the gas diffusion, increasing the pathlength through the MMMs [69]. (3) Rigidification limits the mobility of the polymer chains around the filler particles (at the polymer-filler interface) in comparison to that of the pure polymer [68].

Rigidification only affects a very thin coating of polymer surrounding the filler particles so that permeability does not decrease significantly [68] (the thickness of the rigidified polymer region near the porous particles of zeolite 4A and carbon molecular sieves dispersed in different polymeric matrices have been assumed to be between 2.5 and 20 % of the particle size) [70-73]. This phenomenon also provokes an increase in the gas separation performance because the lower mobility of the polymer chains improves the diffusivity selectivity [68]. (4) Pore blocking by the polymer chains may narrow the pore size of the fillers. Polymer chains are able to fill the pores in various degrees depending on the pore size, restricting the gas passing through the membranes [61, 68]. Even small pores (a few Å in pore diameter) could be affected by this phenomenon, as observed by Li *et al*. [70]. They prepared MMMs with polyethersulfone (PES) as the polymer matrix and zeolite 3A, 4A and 5A as fillers to separate an O_2/N_2 mixture (the kinetic diameter of O_2 is 3.5 Å). It was found that the blocking narrowed the pore of zeolite 5A (4.5 Å) down to *ca*. 4 Å, improving the separation performance [70]. The blocking effect was also demonstrated for zeolite 3A (3 Å) and 4A (3.8 Å); their pores were partially blocked by the PES chains, resulting in a higher resistance to the O_2 transport [70]. Pore blocking is generally accompanied by rigidification (in agreement with the T_g values shown above) and its effect on selectivity depends on the original pore size of the fillers [68]. (5) The clogged sieve occurs when pores are totally blocked by strongly adsorbed molecules (e.g. gas penetrant or solvent coming from the membrane preparation) [74]. The selectivity barely differs although permeability decreases for all the penetrants.

The reduction in the permeability of CO_2 in these gas mixtures ranges between 33 and 50 % for both MMMs. The corresponding values for N_2 and CH_4 are found within 40-50 % and 10-25 %, respectively. These high percentages suggest pore blocking rather than rigidification. The pore blocking is thought to have narrowed the pore size of both fillers in the MMMs below the kinetic dimeter of CO_2 in such a way that the flow of CO_2, CH_4 and N_2 molecules was impeded by a molecular sieving effect and only H_2 was capable of diffusing faster.

As observed in Table S4, the permeabilities of CO_2, N_2 and CH_4 through S13_sph&sh/6FDA-DAM are greater than those through S13_sheet_RT/6FDA-DAM while the value for H_2 is smaller in the case of S13_sph&sh/6FDA-DAM. The amorphous component of S13_sph&sh contributes disordered pores which would hamper the gas flux through S13_sph&sh/6FDA-DAM. Thus a lower permeability of all the gases would be expected through the S13_sph&sh/6FDA-DAM membrane. Also, a higher permeability of CO_2 for S13_sheet_RT/6FDA-DAM than that of S13_sph&sh/6FDA-DAM would be expected because of the higher affinity of S13_sheet_RT (having only sheet crystals and not the amorphous spheres). It is thought that the strong CO_2 adsorption on the pore walls of S13_sheet_RT and the CO_2-CO_2 interactions could hinder the flux through the S13_sheet_RT/6FDA-DAM MMM, obtaining a lower value of permeability in comparison to that of S13_sph&sh/6FDA-DAM which is filled with less CO_2 adsorbent particles (spheres and sheets). This phenomenon also affects the gas flow of the bulkier CH_4 and N_2 molecules, so that the corresponding permeabilities are lower for the S13_sheet_RT/6FDA-DAM membrane. In fact, the permeability of N_2 was reduced by 42 and 50 % for S13_sph&sh/6FDA-DAM and S13_sheet_RT/6FDA-DAM, whereas that of CH_4 fell by 10 and 25 %, respectively, confirming the CO_2 adsorption effect also on the N_2 and CH_4 fluxes through S13_sheet_RT/6FDA-DAM. The orientation in the MMM of the sheet crystals of S13_sheet_RT, parallel to the surface (Figure 6b), increases the barrier effect towards CO_2, N_2 and CH_4 due to the higher tortuosity. The flow of H_2 is less affected by the CO_2 adsorption phenomenon due to its smaller kinetic diameter. Because of this and the fact that S13_sheet_RT/6FDA-DAM does not contain amorphous particles, the H_2 molecules pass faster through this MMM.

As mentioned above, the 6FDA-DAM polymer is known for its high capacity to promote a high permeability of CO_2 with moderate selectivity [64]. In fact, it is more permeable to CO_2 than to H_2, as can be seen in Figure 7, giving an inverse H_2/CO_2 selectivity. Regarding the CO_2/H_2 mixture (Figure 7 and Table S4), a decrease in the selectivity is observed compared to that of

the pure polymer. This is as expected since the permeability of CO_2 is lower while the permeability of H_2 increases for both MMMs. Considering the other gas mixtures (Figure 7 and Table S4), while the CO_2/N_2 selectivity for the MMMs slightly exceeds that of the bare polymer, the CO_2/CH_4 selectivity falls. As the CH_4 molecule is bigger than the N_2 molecule, a greater limitation on the flux of CH_4 would be expected, enhancing the CO_2/CH_4 selectivity. The inclusion of particles of S13_sph&sh and S13_sheet_RT in the polymeric matrix may lead to an improvement in the solubility of the more condensable gas (-162 and -196 °C for CH_4 and N_2) and thus a larger permeability of CH_4 than expected. This is due to the morphology changes at the polymer-filler interface which facilitate the solution of the more condensable gases in the MMM [69]. It is worth noting that the improvement in solubility is more significant for S13_sheet_RT since this filler is more crystalline.

The MMMs act as molecular sieves for the H_2/CH_4 mixture, separating both gas components by size exclusion (Figure 7 and Table S4), as seen with narrow porosity fillers such as titanosilicate JFD-L1 [63] and exfoliated zeolite Nu-6(2) [75] in analogous 6FDA-based copolyimides. The H_2 molecules are able to enter the filler pores and permeate through them whereas the CH_4 molecules are too large to enter the pores and remain at the retentate side. The permeabilities of H_2 and CH_4 are thus higher and lower, respectively, through the MMMs than those through the bare 6FDA-DAM. The permeability of both gases is smaller for S13_sph&sh/6FDA-DAM because the amorphous character of S13_sph&sh hinders the gas flow through its pores, as mentioned above. In consequence, the MMMs increase the H_2/CH_4 selectivity (Figure 7), and the selectivity of S13_sph&sh/6FDA-DAM is higher. This is because the flow of CH_4 decreases by 39 and 5 % while that of H_2 increases by 8 and 18 % for S13_sph&sh/6FDA-DAM and S13_sheet_RT/6FDA-DAM, respectively. The presence of the amorphous spherical particles in the filler of S13_sph&sh/6FDA-DAM constitutes a greater hurdle to the CH_4 molecules, counteracting the lower increase in the flux of H_2. The selectivity is increased 1.8-fold by S13_sph&sh/6FDA-DAM (12.7) and 1.2-fold by S13_sheet_RT/6FDA-DAM (8.9) compared to

the neat membrane (7.2). These results suggest that S13_sph&sh is a potential candidate for incorporation into MMMs for H_2/CH_4 separation while S13_sheet_RT could be embedded into a different polymeric matrix to promote the separation of H_2 from CO_2 by a barrier effect.

4 Conclusions

The synthesis of a new ZIF based on hydroxymethylimidazolate, UZAR-S13 (S13_sph&sh), is reported. In the UZAR-S13 skeleton, Zn^{2+} ions act as nodes while hmIm linkers are the struts that connect nodes through coordination bonds. Morphology and X-ray diffractometry studies revealed that UZAR-S13 contains two distinct phases: amorphous spheres and crystalline sheets. Increasing or diminishing the metal:ligand ratio led respectively to obtaining spheres or sheets only. Flat particles were also obtained when the reaction time and temperature changed. Thus, the reaction parameters had a direct influence on the morphology and presence of amorphous phases, demonstrating that small experimental adjustments could result in the desired product. In spite of their low BET specific surface areas, several UZAR-S13-type materials presented good CO_2 uptakes at low pressures, approaching the uptakes of ZIFs with BET areas about 50 times higher, and notable values at high pressures. Both products were included as fillers in MMMs, where their sheet-shaped crystals could provide benefits in gas separation performance. Four distinct separations were studied (CO_2/N_2, CO_2/CH_4, CO_2/H_2 and H_2/CH_4). The results for the mixtures containing CO_2 demonstrated that the 2D crystals of S13_sph&sh and S13_sheet_RT established strong interactions with the CO_2 molecules, hampering the flow of CO_2, N_2 and CH_4 through the MMMs. This barrier effect was increased by the arrangement of the crystals parallel to the membrane surface, as demonstrated by PXRD and SEM characterization. The decrease in permeability of CO_2, N_2 and CH_4 through S13_sph&sh/6FDA-DAM and S13_sheet_RT/6FDA-DAM was also due to pore blocking by the polymeric chains which narrowed the pore size of both fillers, the smallest H_2 molecule being less affected. Neither UZAR-S13 nor S13_sheet_RT improved the performance of the bare

6FDA-DAM membrane for CO_2 containing mixtures. For the H_2/CH_4 pair, the fillers provoked an increase in the selectivity by a molecular sieving effect with a greater improvement for S13_sph&sh/6FDA-DAM. The amorphous spherical particles of S13_sph&sh restricted the flux of CH_4 to a higher degree, counteracting the lower increase in the flow of H_2 in comparison to that of S13_sheet_RT/6FDA-DAM. UZAR-S13 materials are capable of distinguishing molecules with different kinetic diameters and show strong interaction with CO_2 molecules, allowing their use in membrane-based gas separations.

Acknowledgements

Financial support from the Spanish Ministry of Economy and Competitiveness (MINECO) and FEDER (MAT2013-40556-R, MAT2016-77290-R (MINECO/FEDER) and CTQ2015-66080-R (MINECO/FEDER)), the European Social Fund (ESF) and the Aragón Government (DGA, T05) is gratefully acknowledged. A. P.-C. and J. S.-L. also thank the DGA and MINECO, respectively, for Ph.D. grants. The microscopy work was carried out in the Laboratorio de Microscopías Avanzadas at the Instituto de Nanociencia de Aragón (LMA-INA, Universidad de Zaragoza). The authors would like to acknowledge the use of the Servicio General de Apoyo a la Investigación-SAI (Universidad de Zaragoza).

References

[1] R. Sabouni, H. Kazemian, S. Rohani, Carbon dioxide capturing technologies: a review focusing on metal organic framework materials (MOFs), Environ. Sci. Pollut. Res. 21 (2014) 5427-5449.

[2] Y. Liu, Z.U. Wang, H.-C. Zhou, Recent advances in carbon dioxide capture with metal-organic frameworks, Greenhouse Gases: Sci. Technol. 2 (2012) 239-259.

[3] K. Sumida, D.L. Rogow, J.A. Mason, T.M. McDonald, E.D. Bloch, Z.R. Herm, T.-H. Bae, J.R. Long, Carbon dioxide capture in metal-organic frameworks, Chem. Rev. 112 (2012) 724-781.

[4] P. Serra-Crespo, R. Berger, W. Yang, J. Gascon, F. Kapteijn, Separation of CO_2/CH_4 mixtures over NH_2-MIL-53-An experimental and modelling study, Chem. Eng. Sci. 124 (2015) 96-108.

[5] X. Wu, M.N. Shahrak, B. Yuan, S. Deng, Synthesis and characterization of zeolitic imidazolate framework ZIF-7 for CO_2 and CH_4 separation, Microporous Mesoporous Mater. 190 (2014) 189-196.

[6] K.V. Kumar, G. Charalambopoulou, M. Kainourgiakis, A. Stubos, T. Steriotis, Insights on the physical adsorption of hydrogen and methane in UiO series of MOFs using molecular simulations, Comput. Theor. Chemistry 1061 (2015) 36-45.

[7] C.M. Simon, J. Kim, L.-C. Lin, R.L. Martin, M. Haranczyk, B. Smit, Optimizing nanoporous materials for gas storage, Phys. Chem. Chem. Phys. 16 (2014) 5499-5513.

[8] J.-R. Li, J. Sculley, H.-C. Zhou, Metal-organic frameworks for separations, Chem. Rev. 112 (2012) 869-932.

[9] S.R. Venna, M.A. Carreon, Metal-organic framework membranes for carbon dioxide separation, Chem. Eng. Sci. 124 (2015) 3-19.

[10] M. Shah, M.C. McCarthy, S. Sachdeva, A.K. Lee, H.-K. Jeong, Current status of metal-organic framework membranes for gas separations: promises and challenges, Ind. Eng. Chem. Res. 51 (2012) 2179-2199.

[11] B. Zornoza, C. Tellez, J. Coronas, J. Gascon, F. Kapteijn, Metal-organic framework based mixed matrix membranes: an increasingly important field of research with a large application potential, Microporous Mesoporous Mater. 166 (2013) 67-78.

[12] S. Japip, H. Wang, Y.C. Xiao, T.S. Chung, Highly permeable zeolitic imidazolate framework (ZIF)-71 nano-particles enhanced polyimide membranes for gas separation, J. Membr. Sci. 467 (2014) 162-174.

[13] S. Japip, K.S. Liao, T.S. Chung, Molecularly tuned free volume of vapor cross-linked 6FDA-durene/ZIF-71 MMMs for H2/CO2 separation at 150 °C, Adv. Mater. 29 (2017).

[14] P. Amo-Ochoa, F. Zamora, Coordination polymers with nucleobases: from structural aspects to potential applications, Coord. Chem. Rev. 276 (2014) 34-58.

[15] S. Kitagawa, R. Kitaura, S. Noro, Functional porous coordination polymers, Angew. Chem., Int. Ed. 43 (2004) 2334-2375.

[16] S.L. Qiu, G.S. Zhu, Molecular engineering for synthesizing novel structures of metal-organic frameworks with multifunctional properties, Coord. Chem. Rev. 253 (2009) 2891-2911.

[17] C. Serre, F. Millange, C. Thouvenot, M. Nogues, G. Marsolier, D. Louer, G. Ferey, Very large breathing effect in the first nanoporous chromium(III)-based solids: MIL-53 or $Cr^{III}(OH)\cdot\{O_2C\text{-}C_6H_4\text{-}CO_2\}\cdot\{HO_2C\text{-}C_6H_4\text{-}CO_2H\}_x\cdot H_2O_y$, J. Am. Chem. Soc. 124 (2002) 13519-13526.

[18] K.S. Park, Z. Ni, A.P. Cote, J.Y. Choi, R.D. Huang, F.J. Uribe-Romo, H.K. Chae, M. O'Keeffe, O.M. Yaghi, Exceptional chemical and thermal stability of zeolitic imidazolate frameworks, Proc. Natl. Acad. Sci. U. S. A. 103 (2006) 10186-10191.

[19] B. Chen, Z. Yang, Y. Zhu, Y. Xia, Zeolitic imidazolate framework materials: recent progress in synthesis and applications, J. Mater. Chem. A 2 (2014) 16811-16831.

[20] S.R. Venna, J.B. Jasinski, M.A. Carreon, Structural evolution of zeolitic imidazolate framework-8, J. Am. Chem. Soc. 132 (2010) 18030-18033.

[21] J. Cravillon, R. Nayuk, S. Springer, A. Feldhoff, K. Huber, M. Wiebcke, Controlling zeolitic imidazolate framework nano- and microcrystal formation: insight into crystal growth by time-resolved in situ static light scattering, Chem. Mater. 23 (2011) 2130-2141.

[22] G. Yilmaz, A. Ozcan, S. Keskin, Computational screening of ZIFs for CO_2 separations, Mol. Sim. 41 (2015) 713-726.

[23] A. Phan, C.J. Doonan, F.J. Uribe-Romo, C.B. Knobler, M. O'Keeffe, O.M. Yaghi, Synthesis, structure, and carbon dioxide capture properties of zeolitic imidazolate frameworks, Acc. Chem. Res. 43 (2010) 58-67.

[24] S. Wang, Q. Yang, J. Zhang, X. Zhang, C. Zhao, L. Jiang, C.-Y. Su, Two-dimensional charge-separated metal-organic framework for hysteretic and modulated sorption, Inorg. Chem. 52 (2013) 4198-4204.

[25] S.C. Junggeburth, L. Diehl, S. Werner, V. Duppel, W. Sigle, B.V. Lotsch, Ultrathin 2D coordination polymer nanosheets by surfactant-mediated synthesis, J. Am. Chem. Soc. 135 (2013) 6157-6164.

[26] A.A. Balandin, Thermal properties of graphene and nanostructured carbon materials, Nat. Mater. 10 (2011) 569-581.

[27] J.N. Coleman, M. Lotya, A. O'Neill, S.D. Bergin, P.J. King, U. Khan, K. Young, A. Gaucher, S. De, R.J. Smith, I.V. Shvets, S.K. Arora, G. Stanton, H.Y. Kim, K. Lee, G.T. Kim, G.S. Duesberg, T. Hallam, J.J. Boland, J.J. Wang, J.F. Donegan, J.C. Grunlan, G. Moriarty, A. Shmeliov, R.J. Nicholls, J.M. Perkins, E.M. Grieveson, K. Theuwissen, D.W. McComb, P.D. Nellist, V. Nicolosi, Two-dimensional nanosheets produced by liquid exfoliation of layered materials, Science 331 (2011) 568-571.

[28] T.E. Mallouk, J.A. Gavin, Molecular recognition in lamellar solids and thin films, Acc. Chem. Res. 31 (1998) 209-217.

[29] T. Rodenas, I. Luz, G. Prieto, B. Seoane, H. Miro, A. Corma, F. Kapteijn, F.X. Llabres i Xamena, J. Gascon, Metal-organic framework nanosheets in polymer composite materials for gas separation, Nat. Mater. 14 (2015) 48-55.

[30] W. Wang, J.-Y. Sun, D.-J. Zhang, T.-Y. Song, W. Song, L.-Y. Zhang, Y.-L. Chen, Y. Fan, P. Zhang, New two-dimensional metal-organic frameworks constructed from 1H-

benzimidazole-5,6-dicarboxylic acid with luminescent studies, Inorg. Chim. Acta 384 (2012) 105-110.

[31] C. Rubio, B. Zornoza, P. Gorgojo, C. Tellez, J. Coronas, Separation of H_2 and CO_2 containing mixtures with mixed matrix membranes based on layered materials, Curr. Org. Chem. 18 (2014) 2351-2363.

[32] K. Varoon, X. Zhang, B. Elyassi, D.D. Brewer, M. Gettel, S. Kumar, J.A. Lee, S. Maheshwari, A. Mittal, C.-Y. Sung, M. Cococcioni, L.F. Francis, A.V. McCormick, K.A. Mkhoyan, M. Tsapatsis, Dispersible exfoliated zeolite nanosheets and their application as a selective membrane, Science 334 (2011) 72-75.

[33] K. Nakagawa, D. Tanaka, S. Horike, S. Shimomura, M. Higuchi, S. Kitagawa, Enhanced selectivity of CO_2 from a ternary gas mixture in an interdigitated porous framework, Chem. Commun. 46 (2010) 4258-4260.

[34] A. Perea-Cachero, B. Seoane, B. Diosdado, C. Tellez, J. Coronas, Synthesis, structure and characterization of a layered coordination polymer based on Zn(II) and 6-(methylmercapto)purine, RSC Adv. 6 (2016) 260-268.

[35] Y. Inubushi, S. Horike, T. Fukushima, G. Akiyama, R. Matsuda, S. Kitagawa, Modification of flexible part in Cu^{2+} interdigitated framework for CH_4/CO_2 separation, Chem. Commun. 46 (2010) 9229-9231.

[36] Y. Peng, Y. Li, Y. Ban, H. Jin, W. Jiao, X. Liu, W. Yang, Metal-organic framework nanosheets as building blocks for molecular sieving membranes, Science 346 (2014) 1356-1359.

[37] D. Andirova, C.F. Cogswell, Y. Lei, S. Choi, Effect of the structural constituents of metal-organic frameworks on carbon dioxide capture, Microporous Mesoporous Mater. 219 (2016) 276-305.

[38] L. Wang, Y.M. Cao, M.Q. Zhou, S.J. Zhou, Q. Yuan, Novel copolyimide membranes for gas separation, J. Membr. Sci. 305 (2007) 338-346.

[39] J.H. Kim, S.B. Lee, S.Y. Kim, Incorporation effects of fluorinated side groups into polyimide membranes on their physical and gas permeation properties, J. Appl. Polym. Sci. 77 (2000) 2756-2767.

[40] C.A. Schneider, W.S. Rasband, K.W. Eliceiri, NIH Image to ImageJ: 25 years of image analysis, Nat. Methods 9 (2012) 671-675.

[41] C. Zhang, X.S. Lu, A.Z. Gu, How to accurately determine the uptake of hydrogen in carbonaceous materials, Int. J. Hydrogen Energy 29 (2004) 1271-1276.

[42] T. Kiyobayashi, H.T. Takeshita, H. Tanaka, N. Takeichi, A. Zuttel, L. Schlapbach, N. Kuriyama, Hydrogen adsorption in carbonaceous materials: how to determine the storage capacity accurately, J. Alloys Compd. 330 (2002) 666-669.

[43] R. Banerjee, A. Phan, B. Wang, C. Knobler, H. Furukawa, M. O'Keeffe, O.M. Yaghi, High-throughput synthesis of zeolitic imidazolate frameworks and application to CO_2 capture, Science 319 (2008) 939-943.

[44] S. Bhattacharjee, M.-S. Jang, H.-J. Kwon, W.-S. Ahn, Zeolitic imidazolate frameworks: synthesis, functionalization, and catalytic/adsorption applications, Catal. Surv. Asia 18 (2014) 101-127.

[45] A. Schaate, M. Schulte, M. Wiebcke, A. Godt, P. Behrens, One-dimensional Zn(II) oligo(phenyleneethynylene)dicarboxylate coordination polymers: synthesis, crystal structures, thermal and photoluminescent properties, Inorg. Chim. Acta 362 (2009) 3600-3606.

[46] C. Chen, J. Kim, D.-A. Yang, W.-S. Ahn, Carbon dioxide adsorption over zeolite-like metal organic frameworks (ZMOFs) having a sod topology: structure and ion-exchange effect, Chem. Eng. J. 168 (2011) 1134-1139.

[47] R. Chen, J. Yao, Q. Gu, S. Smeets, C. Baerlocher, H. Gu, D. Zhu, W. Morris, O.M. Yaghi, H. Wang, A two-dimensional zeolitic imidazolate framework with a cushion-shaped cavity for CO_2 adsorption, Chem. Commun. 49 (2013) 9500-9502.

[48] D.F. Liu, Y.B. Wu, Q.B. Xia, Z. Li, H.X. Xi, Experimental and molecular simulation studies of CO_2 adsorption on zeolitic imidazolate frameworks: ZIF-8 and amine-modified ZIF-8, Adsorption 19 (2013) 25-37.

[49] W. Morris, B. Leung, H. Furukawa, O.K. Yaghi, N. He, H. Hayashi, Y. Houndonougbo, M. Asta, B.B. Laird, O.M. Yaghi, A combined experimental-computational investigation of carbon dioxide capture in a series of isoreticular zeolitic imidazolate frameworks, J. Am. Chem. Soc. 132 (2010) 11006-11008.

[50] S.K. Nune, P.K. Thallapally, A. Dohnalkova, C. Wang, J. Liu, G.J. Exarhos, Synthesis and properties of nano zeolitic imidazolate frameworks, Chem. Commun. 46 (2010) 4878-4880.

[51] K.G. Ray, D.L. Olmsted, J.M.R. Burton, Y. Houndonougbo, B.B. Laird, M. Asta, Gas membrane selectivity enabled by zeolitic imidazolate framework electrostatics, Chem. Mater. 26 (2014) 3976-3985.

[52] Y. Lo, C.H. Lam, C.W. Chang, A.C. Yang, D.Y. Kang, Polymorphism/pseudopolymorphism of metal-organic frameworks composed of zinc(II) and 2methylimidazole: synthesis, stability, and application in gas storage, RSC Adv. 6 (2016) 89148-89156.

[53] J. Sanchez-Lainez, B. Zornoza, A. Mayoral, A. Berenguer-Murcia, D. Cazorla-Amoros, C. Tellez, J. Coronas, Beyond the H_2/CO_2 upper bound: one-step crystallization and separation of nano-sized ZIF-11 by centrifugation and its application in mixed matrix membranes, J. Mater. Chem. A 3 (2015) 6549-6556.

[54] S.B. Wang, J.L. Lin, X.C. Wang, Semiconductor-redox catalysis promoted by metal-organic frameworks for CO2 reduction, Phys. Chem. Chem. Phys. 16 (2014) 14656-14660.

[55] Z. Ozturk, J.P. Hofmann, M. Lutz, M. Mazaj, N.Z. Logar, B.M. Weckhuysen, Controlled synthesis of phase-pure zeolitic imidazolate framework Co-ZIF-9, Eur. J. Inorg. Chem. (2015) 1625-1630.

[56] D. Cazorla-Amoros, J. Alcaniz-Monge, M.A. de la Casa-Lillo, A. Linares-Solano, CO_2 as an adsorptive to characterize carbon molecular sieves and activated carbons, Langmuir 14 (1998) 4589-4596.

[57] A. Berenguer-Murcia, D. Cazorla-Amoros, A. Linares-Solano, MCM-41 porosity: are surface corrugations micropores?, Adsorpt. Sci. Technol. 29 (2011) 443-455.

[58] J. Liu, P.K. Thallapally, B.P. McGrail, D.R. Brown, J. Liu, Progress in adsorption-based CO_2 capture by metal-organic frameworks, Chem. Soc. Rev. 41 (2012) 2308-2322.

[59] W.L. Qiu, L.R. Xu, C.C. Chen, D.R. Paul, W.J. Koros, Gas separation performance of 6FDA-based polyimides with different chemical structures, Polymer 54 (2013) 6226-6235.

[60] M. Valero, B. Zornoza, C. Tellez, J. Coronas, Mixed matrix membranes for gas separation by combination of silica MCM-41 and MOF NH_2-MIL-53(Al) in glassy polymers, Microporous Mesoporous Mater. 192 (2014) 23-28.

[61] M.S. Boroglu, A.B. Yumru, Gas separation performance of 6FDA-DAM-ZIF-11 mixed-matrix membranes for H_2/CH_4 and CO_2/CH_4 separation, Sep. Purif. Technol. 173 (2017) 269-279.

[62] B. Zornoza, B. Seoane, J.M. Zamaro, C. Tellez, J. Coronas, Combination of MOFs and zeolites for mixed-matrix membranes, ChemPhysChem 12 (2011) 2781-2785.

[63] A. Galve, D. Sieffert, C. Staudt, M. Ferrando, C. Guell, C. Tellez, J. Coronas, Combination of ordered mesoporous silica MCM-41 and layered titanosilicate JDF-L1 fillers for 6FDA-based copolyimide mixed matrix membranes, J. Membr. Sci. 431 (2013) 163-170.

[64] R.P. Lively, M.E. Dose, L.R. Xu, J.T. Vaughn, J.R. Johnson, J.A. Thompson, K. Zhang, M.E. Lydon, J.S. Lee, L. Liu, Z.S. Hu, O. Karvan, M.J. Realff, W.J. Koros, A high-flux polyimide hollow fiber membrane to minimize footprint and energy penalty for CO_2 recovery from flue gas, J. Membr. Sci. 423 (2012) 302-313.

[65] B. Zornoza, C. Tellez, J. Coronas, O. Esekhile, W.J. Koros, Mixed matrix membranes based on 6FDA polyimide with silica and zeolite microsphere dispersed phases, AIChE J. 61 (2015) 4481-4490.

[66] J.H. Kim, W.J. Koros, D.R. Paul, Effects of CO_2 exposure and physical aging on the gas permeability of thin 6FDA-based polyimide membranes - Part 1. Without crosslinking, J. Membr. Sci. 282 (2006) 21-31.

[67] M.S. Boroglu, M.A. Gurkaynak, Fabrication and characterization of silica modified polyimide-zeolite mixed matrix membranes for gas separation properties, Polym. Bull. 66 (2011) 463-478.

[68] T.-S. Chung, L.Y. Jiang, Y. Li, S. Kulprathipanja, Mixed matrix membranes (MMMs) comprising organic polymers with dispersed inorganic fillers for gas separation, Prog. Polym. Sci. 32 (2007) 483-507.

[69] M. Sadeghi, M.A. Semsarzadeh, H. Moadel, Enhancement of the gas separation properties of polybenzimidazole (PBI) membrane by incorporation of silica nano particles, J. Membr. Sci. 331 (2009) 21-30.

[70] Y. Li, T.S. Chung, C. Cao, S. Kulprathipanja, The effects of polymer chain rigidification, zeolite pore size and pore blockage on polyethersulfone (PES)-zeolite A mixed matrix membranes, J. Membr. Sci. 260 (2005) 45-55.

[71] Y. Li, H.M. Guan, T.S. Chung, S. Kulprathipanja, Effects of novel silane modification of zeolite surface on polymer chain rigidification and partial pore blockage in polyethersulfone (PES)-zeolite A mixed matrix membranes, J. Membr. Sci. 275 (2006) 17-28.

[72] T.T. Moore, R. Mahajan, D.Q. Vu, W.J. Koros, Hybrid membrane materials comprising organic polymers with rigid dispersed phases, AIChE J. 50 (2004) 311-321.

[73] D.Q. Vu, W.J. Koros, S.J. Miller, Mixed matrix membranes using carbon molecular sieves - II. Modeling permeation behavior, J. Membr. Sci. 211 (2003) 335-348.

[74] T.T. Moore, W.J. Koros, Non-ideal effects in organic-inorganic materials for gas separation membranes, J. Mol. Struct. 739 (2005) 87-98.

[75] P. Gorgojo, D. Sieffert, C. Staudt, C. Tellez, J. Coronas, Exfoliated zeolite Nu-6(2) as filler for 6FDA-based copolyimide mixed matrix membranes, J. Membr. Sci. 411-412 (2012) 146-152.

Highlights

- UZAR-S13 is a new ZIF with spherical and 2D particles.
- UZAR-S13 type materials showed good CO_2 uptakes, approaching values of known ZIFs.
- Pore blocking was observed for the 6FDA-DAM MMMs in separation of gas mixtures.
- 2D crystals in MMMs caused a barrier effect to gases due to a strong CO_2 affinity.
- The H_2/CH_4 selectivity was improved by molecular sieving.